Dense versus dilute fluidization of cohesive particles: Reverse sensitivity to friction and restitution coefficient

Peiyuan Liu, Casey Q. LaMarche, Kevin M. Kellogg, and Christine M. Hrenya

Phys. Rev. Fluids **2**, 054302 — Published 31 May 2017
DOI: 10.1103/PhysRevFluids.2.054302

Dense vs. dilute fluidization of cohesive particles: Reverse sensitivity to friction and restitution coefficient

Peiyuan Liu, Casey Q. LaMarche, Kevin M. Kellogg, and Christine M. Hrenya*
Department of Chemical and Biological Engineering, University of Colorado Boulder, Boulder, CO 80309, USA

Abstract

Numerical simulations based on DEM-CFD were conducted to study the behavior of gas-solid flows of cohesive particles under various values of particle friction and restitution coefficient, which dictate the energy dissipation in the tangential and normal directions of particle relative motion. Fluidized beds and riser flows were selected as typical systems for dense and dilute flows, respectively. Based on the defluidization curves and agglomerate properties in respective systems, a reverse dependence on friction and restitution coefficient was identified: defluidization curves were dominated by friction while agglomerates in riser flow were governed by the restitution coefficient. The reverse sensitivity is ascribed to the difference in particle interactions for the two systems. In the fluidized bed, particles primarily interact via enduring multiple-particle contacts, in which the dynamics in the tangential directions dominates. In riser flows, the instantaneous binary collisions are more common and the relative motion of particles in the normal direction becomes important. A non-monotonic response of defluidization curves to varying sliding friction was observed, which is explained by the competing effects of increased sliding and enhanced spin of particles on bed porosity. This study highlights the importance of correct experimental measurement of solid properties for numerical simulations. The results are also useful for driving the development of continuum modeling of gas-solid flows of cohesive particles.

1 Introduction

Gas-solid flows are important phenomena in nature and industry [1-3]. Fluidized beds and risers are common unit operations in a range of industries. Fluidized beds typically run with superficial gas velocities slightly larger than the minimum fluidization velocity, at which the pressure drop of gas phase balances the weight of the solid phase. The relatively low gas-solid drag results in a dense flow with sufficient physical contacts between particles. The dense flow ensures efficient mass and heat transfer and making fluidized beds effective in processes such as coating, drying and granulation [1,4]. On the other hand, riser flows with a much more dilute solid concentration typically operate at superficial gas velocities around the particle terminal velocity. As an essential component of circulating fluidized bed

* Corresponding author.
E-mail address: hrenya@colorado.edu

(CFB), knowledge on the riser flows is crucial to the evaluation of the performance of CFB reactors [5] and particle entrainment [6,7].

Interparticle cohesion originating from van der Waals force and liquid bridging has pronounced effects on gas-solid flows in both fluidized beds and risers. In fluidized beds, a variety of novel behaviors associated with cohesion have been reported, such as the existence of a homogenous fluidization with increased minimum bubbling velocity [8-11], increased pressure drop overshoot [12,13], higher pressure drop fluctuations [14] and reduced bubble size [15]. In riser flows, evident influence of cohesion was also captured. For example, depending on the solid concentration, the interaction between van der Waals force and gas-solid drag can lead to either enhanced or depressed cluster formation close to the wall of the riser [16]. Increased agglomeration was observed for wet particles with capillary force as the dominant mechanism of cohesion [17,18].

The friction and restitution coefficients, which are associated with the energy dissipation during relative motion of particles in tangential and normal directions, respectively, have significant impacts on gas-solid flows as well. Increased dissipation due to higher friction or lower restitution coefficient generally leads to larger "heterogeneity" in gas-solid flows of non-cohesive particles [4,19]. In fluidized beds, heterogeneities (bubbles) are reflected by the increased fluctuations of pressure drop and bed height with increasing friction [20-22], as well as increased bubble size with decreasing restitution coefficient [23,24]. For riser flows, enhanced heterogeneities (clusters) are characterized by the increasing cluster size as a result of increasing friction or decreasing restitution coefficient [16,17,25], though the velocity distribution of particles remains largely unaffected [26].

Since cohesion is known to enhance energy dissipation during particle collisions [13,15,27], studies on the interplay of cohesion with friction and restitution coefficient in fluidized beds are emerging. Using coupled discrete element method and computational fluid mechanics (DEM-CFD) simulations of cohesive particles, Hou et al. [28] found that both sliding and rolling friction contribute to the formation of expanded beds during fluidization. Galvin and Benyahia [29] reported that a larger sliding friction coefficient results in an increasing minimum fluidization velocity. Wilson et al. [30] recently proposed that decreasing restitution coefficient leads to an increasing number of contacts per particle in the fluidized bed, while a non-linear trend is seen relating sliding friction with the number of contacts per particle and bubble velocity.

In this work, we continue to study the sensitivity of fluidized bed and riser flow of cohesive particles to friction and restitution coefficient based on DEM-CFD simulations, where van der Waal force between particles was considered. In particular, we focus on the less explored riser flows, where the solid concentration is much lower than in fluidized beds. Defluidization curves in fluidized beds and agglomerate properties in riser flows, both of which serve as good indicators of system cohesion level [18,29,31-34], are extracted from the simulations. A large parameter space was covered with the effects of both sliding and rolling friction scrutinized. The results of this study (i) highlight the level of importance of the physical parameters in gas-solid flows depends on the system of interest and (ii) provide validation data for continuum model predictions incorporating particle cohesion and friction, a subject of enduring theoretical effort [35-41].

2 Numerical method and simulation conditions

2.1 DEM-CFD

Numerical simulations based on DEM-CFD were conducted in this study so that particle friction and restitution coefficient are varied individually without affecting other material properties. In DEM-CFD, the solid phase is treated as discrete particles whose trajectories are solved by Newton's equations of motion, given by

$$m\frac{d\mathbf{v}}{dt} = \mathbf{F}_c + \mathbf{F}_f + \mathbf{F}_{vdW} + m\mathbf{g} \tag{1}$$

$$I\frac{d\boldsymbol{\omega}}{dt} = \mathbf{R}\times\mathbf{F}_c^t - \mu_r R F_c^n \hat{\boldsymbol{\omega}} \tag{2}$$

where m, $\mathbf{v}$, I and $\boldsymbol{\omega}$ are, respectively, the particle mass, translational velocity, moment of inertia and angular velocity. $\mathbf{R}$ is a vector aligned from particle center to the contact point with its magnitude equal to particle radius R. $\mathbf{F}_c$, $\mathbf{F}_f$, and $\mathbf{F}_{vdW}$ are, respectively, the total contact force, particle-fluid drag and van der Waals force (cohesion). The first and second terms on the right-hand side of Eq. (2) represent torques due to tangential contact force and rolling resistance, respectively, where μ_r is the rolling friction coefficient [42,43]. The contact force $\mathbf{F}_c$ is calculated by the visco-elastic model [44] in both normal and tangential directions. The magnitude of the normal contact force F_c^n between particle i and j is given by

$$F_c^n = \frac{4E_{eff}\sqrt{R_{eff}}}{3}\delta_n^{\frac{3}{2}} + \eta_n\frac{d\delta_n}{dt} \tag{3}$$

where $E_{eff} = 1/[(1-\nu_i^2)/E_i + (1-\nu_j^2)/E_j]$, E is Young's modulus, ν is the Poisson's ratio, $R_{eff} = R_iR_j/(R_i + R_j)$ is the effective radius and δ_n is the normal geometric overlap. F_c^n in Eq.(3) contains two terms. The first term represents the repulsion due to elastic deformation described by the Hertz contact model. The second term represents a viscous damping responsible for the energy dissipation in the normal direction during particle collisions. The normal damping coefficient η_n is related to the restitution coefficient e for binary collisions between non-cohesive particles by [45]

$$\eta_n = \frac{-2\sqrt{15}R_{eff}^{\frac{1}{4}}\sqrt{m_{eff}E_{eff}}\ln e}{3\sqrt{\pi^2 + \ln^2 e}}\delta_n^{\frac{1}{4}} \tag{4}$$

where $m_{eff} = m_im_j/(m_i + m_j)$ is the reduced mass. The corresponding contact force in the tangential direction F_c^t is given by

$$F_c^t = \begin{cases} \frac{16G_{eff}\sqrt{R_{eff}}}{3}\delta_n^{\frac{1}{2}}\delta_t + \eta_t \frac{d\delta_t}{dt} & F_c^t < \mu_s F_c^n \\ \mu_s F_c^n & F_c^t \geq \mu_s F_c^n \end{cases} \tag{5}$$

where $G_{eff} = 1/[(2 - \nu_j)/G_i + (2 - \nu_i)/G_j]$, $G_k = E_k/[2(1 + \nu_k)]$, $(k = i, j)$ is shear modulus and δ_t is the tangential displacement during particle collisions. The tangential damping coefficient η_t is commonly assumed equal to η_n [44]. In this work, we set $\eta_t \equiv \eta_n(e = 0.97)$ when we vary e in the simulations, since changing η_t within the range $\eta_n(e = 0.97) \leq \eta_t \leq \eta_n(e = 0.4)$ has little impact on simulation results. Sliding friction is turned on whenever F_c^t exceeds that maximum static friction approximated to be $\mu_s F_c^n$, where μ_s is the sliding friction coefficient. Particle-wall contacts are treated similarly as particle-particle interactions. Description on the cohesion model for van der Waals force F_{vdW} is detailed in our recent work (section 3.2 in ref. [34] and ref. [46]), where F_{vdW} is expressed as a function of particle radius R, Hamaker constant A, interparticle separation distance D and parameters quantifying surface roughness in terms of root-mean-square amplitudes and wavelengths. As the separation distance reduces below the intermolecular separation [47], F_{vdW} remains constant i.e. $F_{vdW} \equiv F_{vdW}(D_0)$ for $D \leq D_0$, similarly to previous studies summarized recently by Guo and Curtis [48]. The particle-fluid interaction force $\mathbf{F}_f$ is given by

$$\mathbf{F}_f = -V\nabla P_g - \frac{V\beta}{1-\varepsilon}\left(\mathbf{v}_g - \mathbf{v}\right) \tag{6}$$

where V is the volume of the particle, P_g is the gas pressure, β is the gas-solid frictional coefficient, $\mathbf{v}_g$ is the gas velocity, and ε is the porosity. β can be obtained from different drag models. In this work, the model developed by Hill et al. [49,50] based on Lattice–Boltzmann simulations with the application range extended by Benyahia et al. [51] to cover the full range of porosity in fluidized beds was applied.

The gas phase is solved using CFD with the continuity and momentum equations given by

$$\frac{\partial \varepsilon}{\partial t} + \nabla \cdot \left(\varepsilon \mathbf{v}_g\right) = 0 \tag{7}$$

$$\frac{\partial(\varepsilon \rho_g \mathbf{v}_g)}{\partial t} + \nabla \cdot \left(\varepsilon \rho_g \mathbf{v}_g \mathbf{v}_g\right) = -\varepsilon \nabla P_g + \nabla \cdot \tau_g + \varepsilon \rho_g \mathbf{g} - \mathbf{I}_{gs} \tag{8}$$

where $\boldsymbol{\tau}_g$ is the gas shear stress tensor and $\mathbf{I}_{gs}$ is the gas-solid momentum transfer, given by

$$\mathbf{I}_{gs} = \frac{1}{V_m}\sum_{i=1}^{N_m}\frac{\phi_i^m V\beta}{1-\varepsilon}\left(\mathbf{v}_i - \mathbf{v}_g\right) \tag{9}$$

where V_m is the volume of a CFD cell m and N_m is the number of particles in the cell. The interpolation factor ϕ determines the contribution of the drag force of each particle to the cell, which is inversely proportional to the distance from particle location to the cell center. Refer to Patankar [52] for more details about the CFD solver based on the control volume formulation.

2.2 Simulation conditions

The systems studied in simulations are illustrated in Fig. 1. In the fluidized bed with a square distributor plate (Fig. 1a), defluidization is conducted via a step-wise decreasing superficial gas velocity from $U = 2.0$ to 0 cm/s, with a step size of 0.1 cm/s. To minimize the wall effect, we set side walls to be free-slipping for the gas phase, and frictionless and non-cohesive for the solid phase, similar to our recent work for non-cohesive particles [53]. Each gas velocity is maintained for 0.1 s, sufficient for the relaxation of gas pressure into steady state [34,53]. During defluidization, the flow transits from bubbling to static regimes with the majority of particles accumulating near the bottom of the fluidized bed, resulting in a dense gas-solid flow with solid concentration $\varepsilon_s > 0.4$. The defluidization curves, the gas pressure drop normalized by particle weight pressure as a function of superficial gas velocity, are extracted for data comparison (Section 3.1).

In riser flows with the same dimension as the fluidized bed (Fig. 1b), a dilute gas-solid flow with $\varepsilon_s = 0.01$ is driven by a superficial gas velocity of $U = 51.5$ cm/s. Cyclic boundary conditions are implemented in all directions for both gas and solid phases, similar to previous setups in literature [16,17,54]. Due to particle cohesion, agglomerates form and break in the riser during particle collisions. To track the time evolution of agglomerates, the contact durations between particles t_c were recorded. A particle is included to an agglomerate when its t_c with another particle or agglomerate exceeds a critical value $t_{c,crit}$. In this work, we set $t_{c,crit} = 5.9 \times 10^{-5}$ s, which is 3-5 times t_{cb}, the contact duration for a binary collision with typical impact velocities (relative velocities between approaching particles) in the riser (1-10 cm/s, see Fig. 8c. t_{cb} can be evaluated by Eq. (A3)). As t_{cb} is finite except for agglomeration where t_{cb} diverges in binary collisions [34], $t_c > t_{c,crit}$ is considered an appropriate criterion to claim an agglomeration event. The breakage of agglomerates subject to the collisions with higher impact velocities are also recorded. Specifically, particles are removed from an agglomerate the moment they travel outside the "cohesive well D_c", i.e. when $D > D_c$, where D_c is solved by $\int_0^{D_c} F_{vdW}(D)dD \Big/ \int_0^{\infty} F_{vdW}(D)dD = 99\%$. The robustness of algorithm above is demonstrated by (i) the increase in agglomeration with increasing cohesion and (ii) no agglomeration event detected when cohesion is turned off. Starting from randomly generated positions without overlap, particles in the riser accelerate upwards under particle-fluid interaction until ~ 0.2 s of simulation when the flow becomes fully developed, indicated by the vanishing gradients for the time-averaged velocity profiles of gas and solid phases. The time-averaged particle speed and agglomerate properties over a period of 0.8 s during the fully-developed regimes are collected for data comparison in Section 3.2.

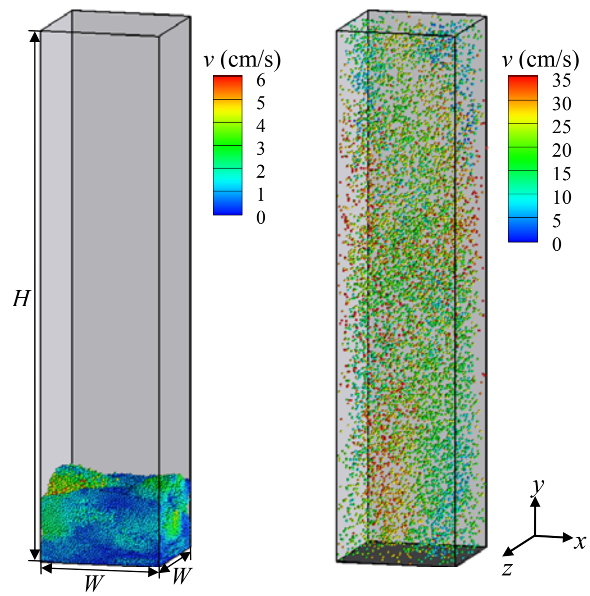

Fig. 1. Systems used in simulations: (a) fluidized bed at U = 1.5 cm/s and (b) riser at U = 51.5 cm/s. The contour indicates particle speed v. (μ_s = 0.275, μ_r = 0, e = 0.97)

It is worth noting that wall effects are minimized in both fluidized bed and riser simulations using the boundary conditions detailed above. This treatment will allow us to conduct direct comparison between simulation results and experiments in future studies. Namely, by using frictionless side walls, the simulations predictions for the complete fluidization velocity U_{cf} (to be discussed in Section 3.1) were previously found to be independent of system size [34]. This system-size independence is key since DEM-CFD simulations are so computationally expensive that the simulation of lab-scale fluidized beds is impossible even with today's high-performance computing. However, a direct quantitative comparison is justified between DEM-CFD simulations with bed width = 0.32 cm (identical to the current simulations) and lab-scale experiments [34], since the results of both are system-size independent. Simulations taking wall effects into account were also conducted, i.e. applying frictional walls for the solid phase and no-slip walls for the gas phase. It is found that simulations with wall effects lead to the same trends as the simulations with minimized wall effects (to be discussed in Section 3.1). Quantitatively, wall effects also have relatively small impact (< 6%) on the simulation results in terms of U_{cf}. The reason lies in the relatively high bed width to particle size ratio of 46.4 used in this work, where a dominant proportion of particles are away from the walls thus not directly subject to wall effects, similar to previous observations [55,56].

Similarly, in riser simulations, wall effects are removed here in order to allow for future comparison with riser experiments. Measurement of agglomerate size distribution will be conducted in the fully-developed region close to the central axis of the bed, where gradients of gas velocities are vanishing. Accordingly, wall effects in simulations need to be minimized to match the velocity profiles in experiments in a posteriori manner. Note that with the presence of walls, a core annular profile is commonly observed [57,58], where the riser exhibits a relatively dilute gas-solid flow at the core and a dense flow near the walls. Depending on the superficial gas velocity and solid flux, a downward flow with enhanced particle clustering can be found close to the walls [59]. Thus, to make direct comparisons between simulations and experiments, we need to make sure the measurements at the core is not subject to non-negligible influence from the side walls. Otherwise, simulations for the full geometry of the riser considering no-slip and frictional walls are necessary. However, a comparison of current results with corresponding simulations that take wall effects into account shows that the qualitative findings of this work remain unaffected.

The parameters used in simulations are summarized in Table 1. the values associated with surface roughness used in the cohesion model are detailed in ref. [34]. For purposes of assessing the relevant physics in the current systems. The pertinent dimensionless groups for gas-solid flows of cohesive particles are also computed and summarized in Table 1, including particle-to-gas density ratio ρ_p/ρ_g, granular Bond number Bo = F_{vdW}/mg, solid concentration ε_s and particle Reynolds number Re_p [60,61]. In defluidization, $\mathrm{Re}_p = d_pU\rho_g/[\mu_g(1-\varepsilon_s)]$ [50], while $\mathrm{Re}_p = d_pv_t\rho_g/\mu_g$ in riser flows, where $v_t = \tau_p g$ is the particle terminal velocity in undisturbed gas flow and $\tau_p = \rho_p d_p^2/(18\mu_g)$ is the particle response time scale [61]. Note while the ρ_p/ρ_g is fixed, ε_s decreases from ~ 0.5 to 0.01; Bo and Rep increases by approximately an order of magnitude from fluidized bed to riser flows, serving as the major differences between the two systems. The simulation results are collected by varying particle sliding friction coefficient from 0.0-1.0 [62], rolling friction coefficient from 0.0 to 0.02 [63,64] and restitution coefficient from 0.4-0.99 [65,66], which are within typical ranges of the materials properties of common solids. The open source solver Multiphase Flow with Interphase eXchanges (MFIX) was used to perform DEM-CFD simulations [67].

Table 1: Parameters in simulations

System dimensions	**Fluidized bed**	**Riser**
Height, H (cm)	1.5	
Width, W (cm)	0.32	
Total number of particles, N_p	50000	9000
Particle properties		
Diameter, d_p (μm)	69	
Density, ρ_p (kg/m^3)	2500	
Young's modulus, E (MPa)	10	
Poisson ratio, v	0.22	
Sliding friction coefficient, μ_s	0 - 1.0	
Rolling friction coefficient, μ_r	0 - 0.02	
Restitution coefficient, e	0.4 - 0.99	
Hamaker constant, A (J)	3.1×10^{-20}	3.1×10^{-19}
Intermolecular separation, D_0 (nm)	0.3	
Gas properties		
Density, ρ_g (kg/m^3)	0.97	

Viscosity, μ_g (kg·m^{-1}·s^{-1})	1.8335×10^{-5}	
Superficial gas velocity, U (cm/s)	0 - 2.0	51.5
Dimensionless groups		
Particle-to-gas density ratio, ρ_p/ρ_g	2577.3	
Granular Bond number, Bo	5.43	54.3
Solid concentration, ε_s	~ 0.5	0.01
Particle Reynolds number, Re_p	0 - 0.15	1.30

3 Results and Discussion

3.1 Defluidization of particles in the fluidized bed

3.1.1 Effect of friction

The effect of friction is first discussed by using a constant restitution coefficient at e = 0.97. The representative flow patterns during defluidization are compared in Fig. 2 at different sliding friction coefficient μ_s. Rolling friction in these simulations is turned off. The transition from the bubbling regime at superficial gas velocity U = 1.6 cm/s to the static regime at U = 0.4 cm/s is observed for all values of μ_s by the reduction of particle speed. However, at U = 1.0 cm/s, while flows with μ_s = 0.02 and μ_s = 0.8 are bubbling, a static bed is seen for particles with an intermediate μ_s = 0.275; this intermediate friction coefficient is also characterized by the tallest bed height at U = 0.4 cm/s, suggesting that increasing μ_s has a non-monotonic effect on defluidization.

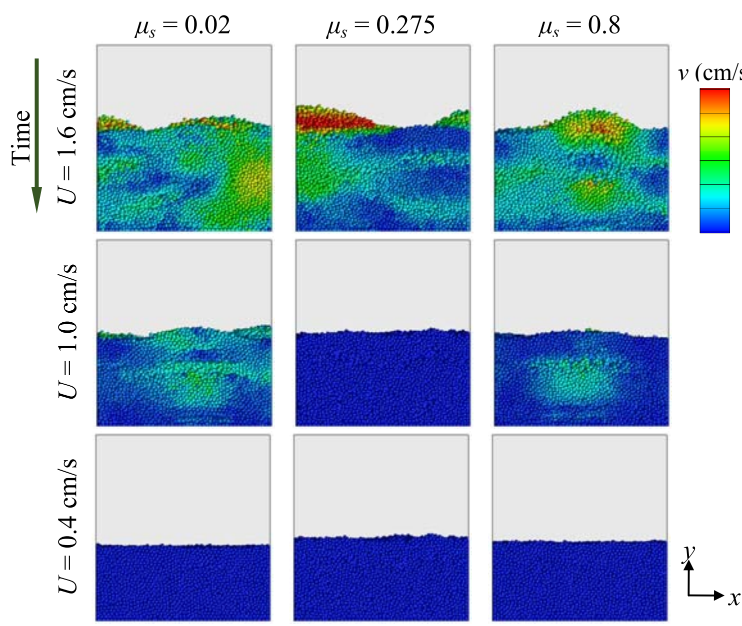

Fig. 2. Flow patterns during defluidization at different μ_s and U. The contour indicates particle speed v. (μ_r = 0, e = 0.97)

A more quantitative assessment of this non-monotonic behavior is possible via defluidization curves, which are plotted in Fig. 3a for cases with $\mu_r = 0$ (bottom plot) corresponding to the snapshots in Fig. 2, and $\mu_r = 0.02$ (top plot). The gas pressure drop normalized by particle weight pressure Δp^* stays at unity for higher U where particles are fully fluidized. With U further reduced, Δp^* decreases and cannot fully support the solid phase (partially fluidized regime). Instead of a linear dependency as is the case for non-cohesive particles, Δp^* shows a non-linear decrease with U due to the varying bed porosity at different U for cohesive systems [29,53,68]. Both μ_s and μ_r affect the defluidization curves in the partially fluidized regime. To quantify the effect of μ_s and μ_r, the complete fluidization velocity U_{cf}, defined as the critical U at which Δp^* fall below 0.98 (marked by vertical lines in Fig. 3a) [34], is plotted as a function of μ_s at different μ_r in Fig. 3b. Similar to the flow pattern evolutions in Fig. 2, U_{cf} exhibits a non-monotonic relation with increasing μ_s in Fig. 3b, where after a relatively sharp increase before $\mu_s \approx 0.2$, U_{cf} drops gradually with the rate of decay reducing with increasing μ_r.

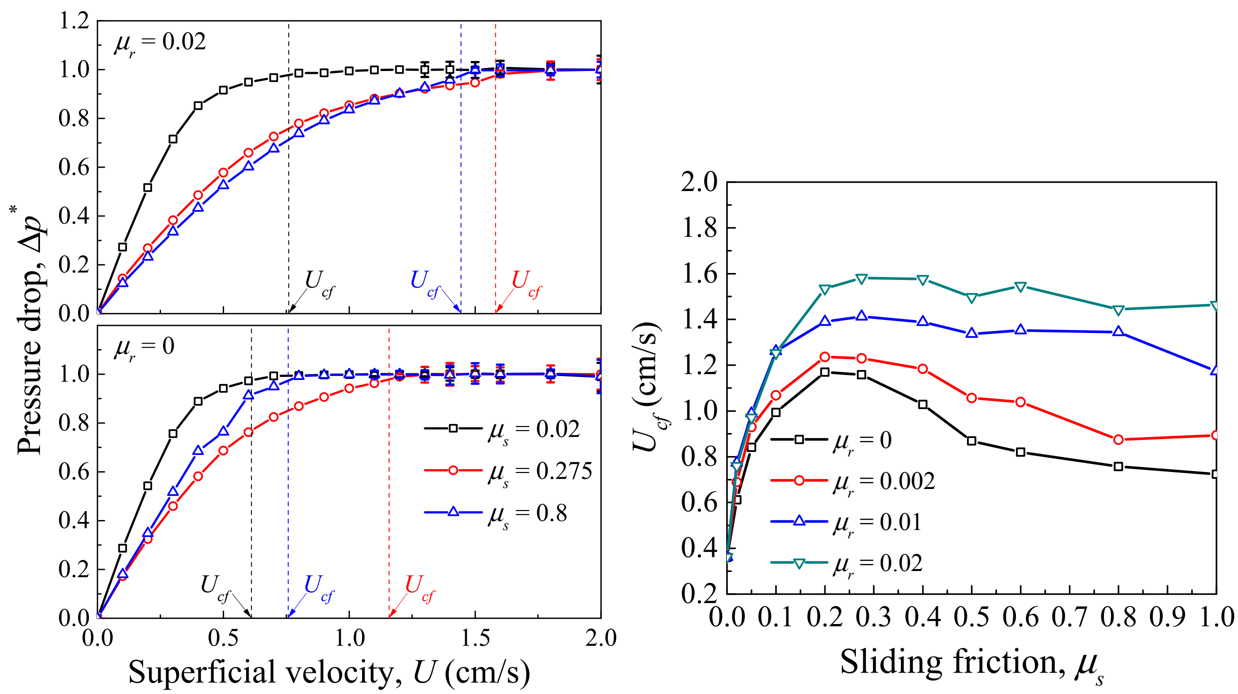

(a) (b)

Fig. 3. (a) Defluidization curves at different μ_s with $\mu_r = 0$ (bottom) and $\mu_r = 0.02$ (top) (Error bars represent standard deviation and can be smaller than symbol size, same for following figures), (b) complete fluidization velocity as a function of μ_s at different μ_r. ($e = 0.97$)

Changing bed porosity ε was found responsible for the variation of U_{cf}. Namely, a higher U_{cf} is required for a more porous bed due to the reduced drag force (which balances bed weight) [10,29,34]. As shown in Fig. 4a (bottom plot), at $\mu_r = 0$, increasing μ_s can increase (μ_s from 0.02 to 0.275) or decrease (μ_s from 0.275 to 0.8) ε at partial fluidization (corresponding to the range $U < U_{cf}$), which directly accounts for the non-monotonic trend between U_{cf} and μ_s in Fig. 3b. However, the decrease of ε

with increasing μ_s is not expected as a higher μ_s is generally considered favorable for stabilizing more porous packings [69-71].

To shed light on the counterintuitive, non-monotonic trend between μ_s and ε, we analyze the translational and angular speeds of the particles with varying μ_s. Two competing effects are identified with increasing μ_s: (i) increased dissipation due to sliding between particles, and (ii) increased driving force for particle spin. For systems without rolling friction (Fig. 4a), at lower μ_s from 0.02 to 0.275, increasing μ_s results in reduced translational speed of particles (Fig. 4a, middle plot), suggesting increased dissipation due to sliding (Effect I). Thus a more porous packing is formed due to limited particle rearrangement at higher μ_s. As μ_s varies from 0.275 to 0.8, due to increased maximum static friction, the condition for sliding is harder to satisfy, as recently shown by Wilson et al [30]. Consequently, Effect I is counterbalanced by Effect II, causing an increase of particle angular speed (Fig. 4a, top plot). With a higher angular speed, particles can roll across each other towards a less porous packing seen in Fig. 4a (bottom plot). Turning on rolling friction to limit particle spin (Fig. 4b, top plot) weakens Effect II, so that Effect I dominates and recovers the monotonic increase of ε with μ_s at partial fluidization (Fig. 4b, bottom plot). Theoretical understanding of the competing effects of μ_s is demonstrated via modeling of simple systems characteristic of the defluidization process in Appendix. Increasing μ_s has also been reported to have non-monotonic effects on bubbling velocity, contact number [30] and minimum bubbling velocity [28] for cohesive particles, to which the mechanism above may partially contribute.

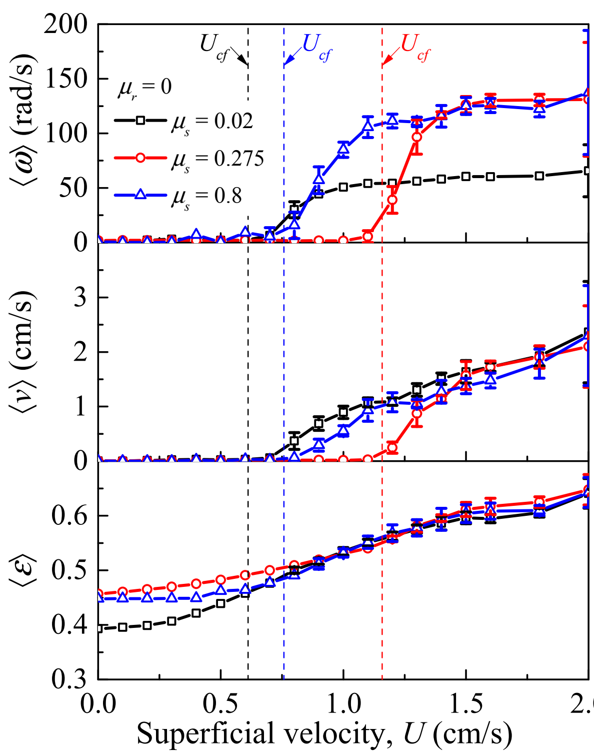

(a)

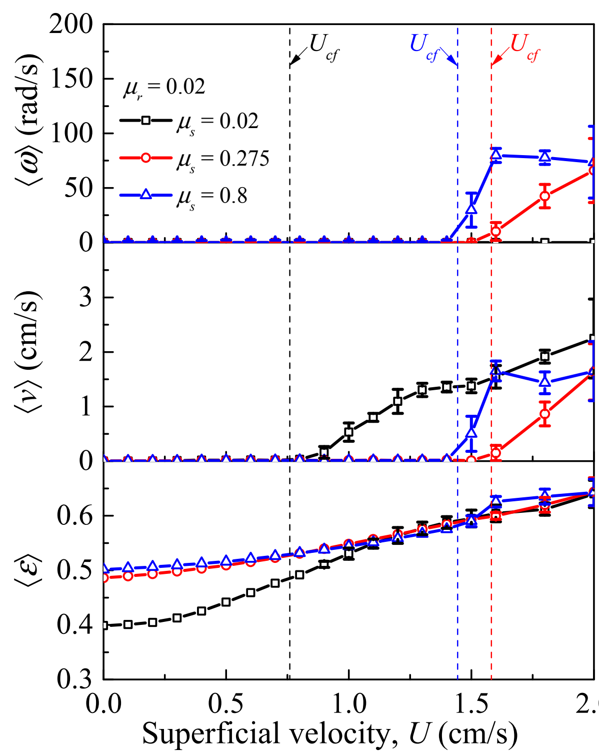

(b)

Fig. 4. Average bed porosity $\langle \varepsilon \rangle$, particle translational speed $\langle v \rangle$ and angular speed $\langle \omega \rangle$ during defluidization at different μ_s for (a) $\mu_r = 0$ and (b) $\mu_r = 0.02$. ($e = 0.97$)

3.1.2 Effect of restitution coefficient

By maintaining a constant $\mu_s = 0.275$ and increasing restitution coefficient e, the defluidization curves largely collapse except at the largest e shown in Fig. 5a. A slight decreasing trend of U_{cf} with increasing e is observed in Fig. 5b, since increasing e leads to decreased dissipation in particle collisions and thus a higher average particle speed. As discussed in the last section, particles with higher velocities have more energy to rearrange towards a tighter packing and correspondingly a decrease in U_{cf}, similar to the consequence of increasing material Young's modulus [15,34,72]. However, compared with friction, the sensitivity of defluidization curves to e is much weaker as U_{cf} varies less than 20% with varying e (Fig. 5b), much smaller than a factor of 3-5 change in U_{cf} with varying μ_s (Fig. 3b). Similar conclusions were also drawn for non-cohesive particles [73,74]. A physical understanding of the reduced sensitivity to e is proposed as follows: due to the high solid concentration in the fluidized bed, particle interactions are dominated by lasting contacts with low impact velocities, especially around U_{cf} where bubbling is beginning to cease. Therefore, with reduced impact velocities, the effect of collisional dissipation (viscous damping) associated with e becomes secondary to frictional interaction. To verify the hypothesis above, we extracted the normal impact velocity distributions $f(v_{im,n})$ in simulations for $\mu_s = 0.275$, $\mu_r = 0$ at $e = 0.97$. Similar to our previous observations [34], as $U \rightarrow U_{cf}$, we found over 80% of the normal impact velocities between particles are lower than the critical agglomeration velocity v_{crit}, below which particles agglomerate together to form lasting contacts (results out shown. More discussion on $f(v_{im,n})$ and v_{crit} is available in the following section).

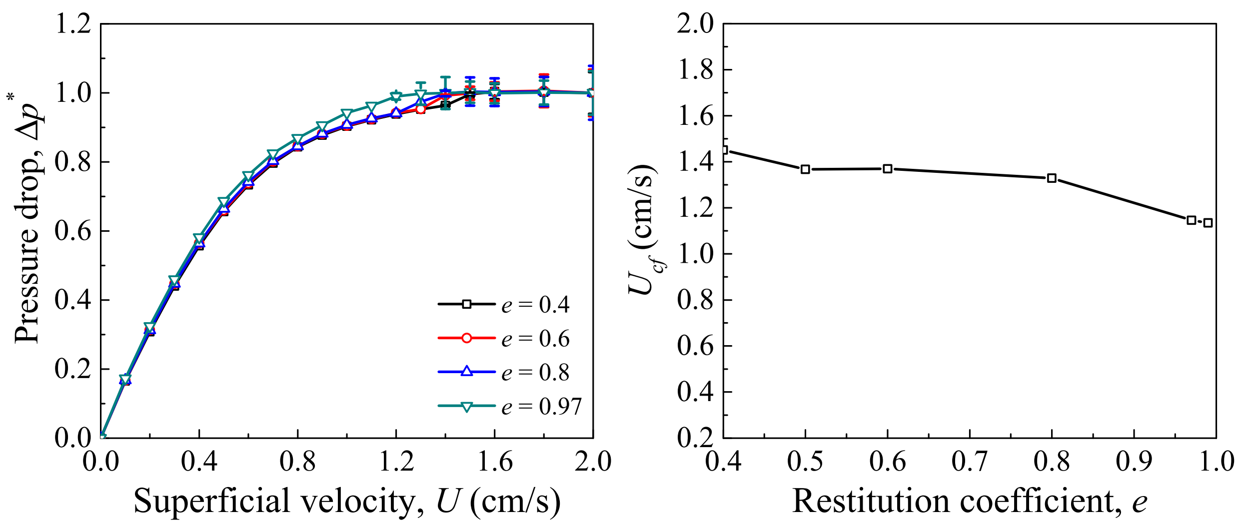

(a) (b)

Fig. 5. (a) Defluidization curves at different e and (b) complete fluidization velocity as a function of e. ($\mu_s = 0.275$, $\mu_r = 0$)

3.2 Agglomerate properties in the riser flow

3.2.1 Effect of restitution coefficient

For riser flow, we first consider the effect of the restitution coefficient, since it is found to have a larger impact than friction. Snapshots of riser flows in the fully-developed regimes with different e at μ_s = 0.275 are compared in Fig. 6. At lower e = 0.4 (Fig. 6a), a high non-uniformity of solid concentration is seen as particles clump together throughout the domain. From the enlarged view with singlets in the system removed in Fig. 6a, a large number of agglomerates N_{agg} are collected with a wide distribution of agglomerate size n_{agg}, i.e. number of particles in an agglomerate. Bigger agglomerates are seen to have smaller translational speed v with two examples circled in the enlarged view in Fig. 6a. At higher e_n = 0.97 (Fig. 6b), while the flow also shows spatial inhomogeneity of local solid concentration, the pattern of inhomogeneity is more reminiscent of hydrodynamic clustering [75,76] where persistent particle contacts and agglomeration are less common (see Section 2.2 for agglomeration criterion). As a result, only a handful of doublets are collected as revealed in the enlarged view in Fig. 6b. The statistical distributions of agglomerate size are summarized in Fig. 6c with varying e. In all distributions, the frequencies of agglomerates decay monotonically with agglomerate size n_{agg} and are well described by $\log[f(n_{agg})] = a[\log(n_{agg})]^b$ with a and b being fitting parameters. As e reduces, tails of the distributions extend to larger n_{agg}. At e = 0.4, big agglomerates consisting of ~ 30 particles are recorded, though the fraction of doublets with n_{agg} = 2 still exceeds 60%. These results are useful for validating continuum models incorporating a population balance [36,77] to consider the effect of agglomerates for dilute gas-solid flows of cohesive particles. Comprehensive validations of continuum models via comparison with DEM-CFD simulations are outside the scope of current work and will be discussed in a future study.

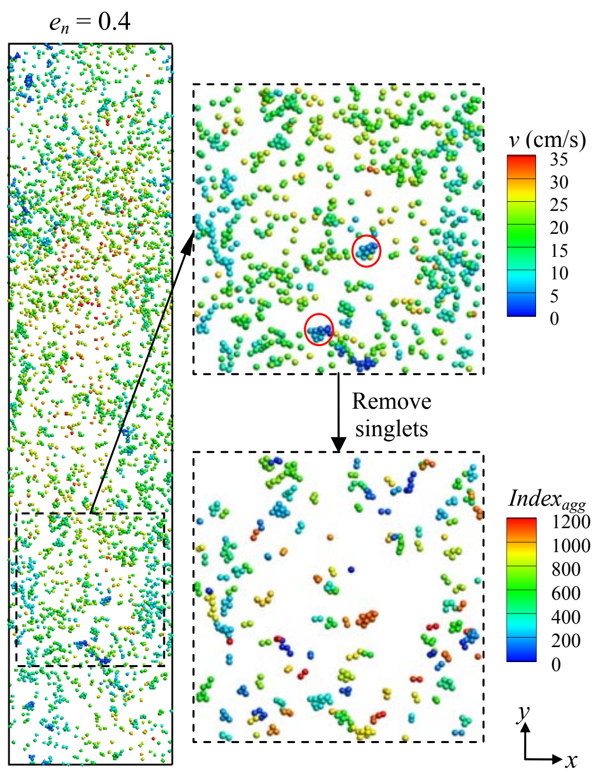

(a)

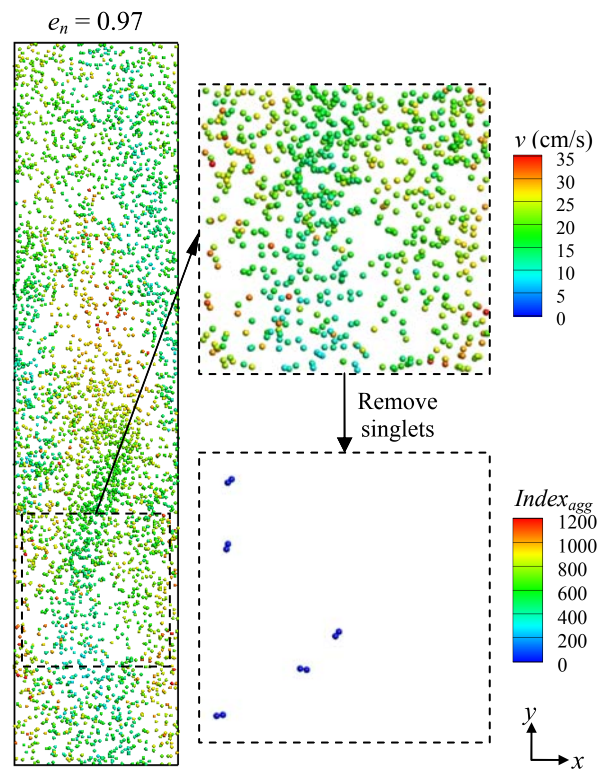

(b)

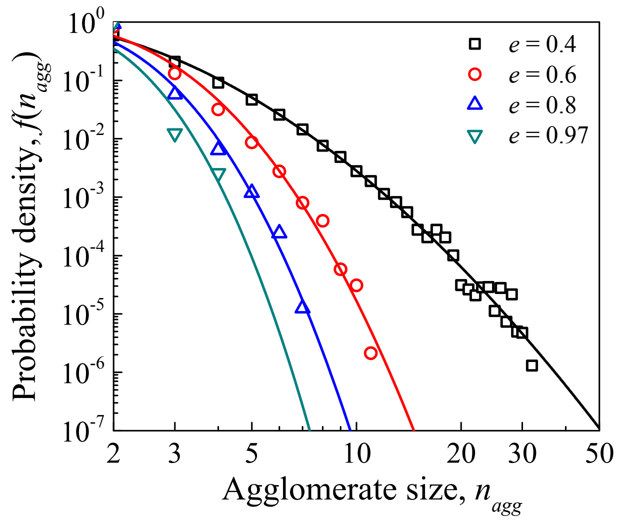

(c)

Fig. 6. Instantaneous flow patterns and visualizations of agglomerates within a layer 10 d_p deep in the riser using (a) $e = 0.4$ and (b) $e = 0.97$. The $index_{agg}$ assigns each agglomerate a number so that they can be differentiated from each other by the color contour; (c) distributions of agglomerate size at different e. Solid lines shows fittings using $\log[f(n_{agg})] = a[\log(n_{agg})]^b$ with a and b as fitting parameters (For e =

0.4, 0.6, 0.8, 0.97, a = -2.55, -4.78, -7.32, -10.17 and b = 1.89, 2.50, 2.55, 2.59, respectively). (μ_s = 0.275, μ_r = 0)

The effect of e on time-averaged properties in fully-developed risers are summarized in Fig. 7. Decreasing e leads to a growth in the total number of agglomerates $\langle N_{agg} \rangle$ and agglomerate size $\langle n_{agg} \rangle$ (Fig. 7, middle and top plot). As larger agglomerates have smaller velocities (Fig. 6a), a reduction in average particle speed $\langle v \rangle$ is observed with decreasing e (Fig. 7, bottom plot), which is different from the non-cohesive particles showing little dependence of particle velocity distribution on e [26]. The reduced $\langle v \rangle$ with decreasing e can be understood by an analysis on the drag force. The results for Fig. 7 are extracted during fully-developed riser flows, where $\langle v \rangle$ and agglomerate properties ($\langle N_{agg} \rangle$ and $\langle n_{agg} \rangle$) reach statistical steady state. In the fully-developed regime where particles reach their terminal velocities, the gravity acting on each particle is balanced by the interaction force from the gas phase so that $m\mathbf{g} = \mathbf{F}_{drag}/(1 - \varepsilon_s)$, where m is particle mass, $\mathbf{F}_{drag}$ is the drag force and ε_s (= 1% in this work) is solid concentration for the entire domain [78]. $\mathbf{F}_{drag}$ increases with the growing magnitude of slip velocity $v_{slip} = |\mathbf{v}_g - \mathbf{v}|$, where $\mathbf{v}_g$ and $\mathbf{v}$ are the gas and particle velocities, respectively. Since a larger pressure drop is required for gas to squeeze through regions with higher local solid concentration, gas tends to bypass agglomerates, leaving a smaller v_g for particles in agglomerates, as confirmed in numerical simulations [61,79] and experiments [80]. In our simulations, the "gas bypassing" phenomenon is also observed by comparing the spatial distributions of bed porosity $\varepsilon = 1 - \varepsilon_s$ and vertical gas velocity v_{gy} ($v_{gy} \approx v_g$ since gas flux is applied in the vertical direction). We found the locations with lower ε (representing agglomerates) coincide with lower v_{gy} (plots not shown for brevity). As a result, the velocities of particles in agglomerates lowers such that v_{slip} can still balance weight of particles. Therefore, as agglomeration increases with decreasing e, the mean particle speed $\langle v \rangle$ decreases. The reduction of particle speed at enhanced agglomeration was also reported by Girardi et al. [18], who changed particle cohesion to control the agglomerate size in DEM-CFD simulations. Through particle-resolved direct numerical simulations, Mehrabadi et al. [81] recently reported a reduction of drag force at the presence of particle clusters compared with uniform particle configurations under the same Re_p and ε_s. Since the drag model used in current work is established under homogeneous distribution of particles, the effect of agglomerates on the drag may not be fully captured. Therefore, in future numerical studies, it will be more appropriate to incorporate a robust structure-dependent drag model, which is under active development [81-84]. However, as the drag reduction is more significant at smaller e with enhanced agglomeration, the qualitative trend that $\langle v \rangle$ reduces with decreasing e is expected to remain valid with the structure-dependent drag considered (larger v_{slip} or smaller v needed for cases with more agglomerates).

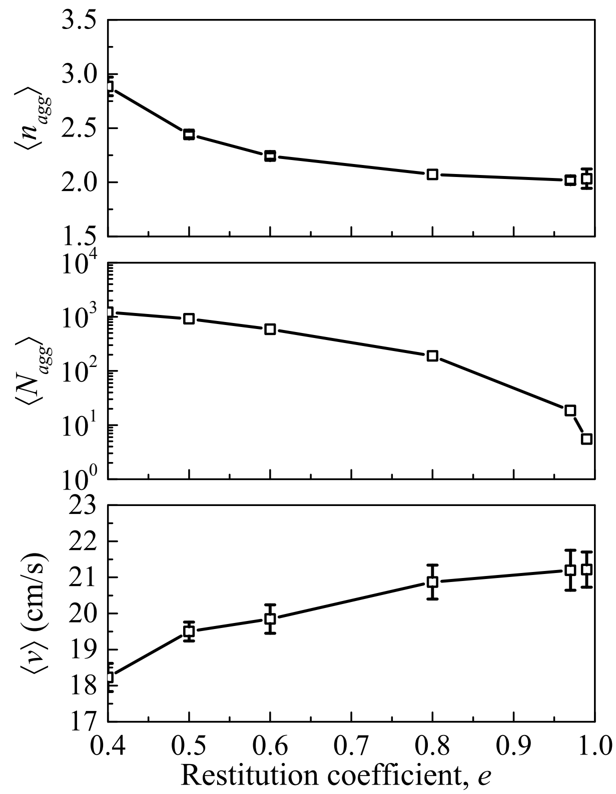

Fig. 7. Time-averaged particle speed $\langle v \rangle$ and agglomerate properties (total number of agglomerates $\langle N_{agg} \rangle$ and agglomerate size $\langle n_{agg} \rangle$) as a function of e. Note the log scale used for $\langle N_{agg} \rangle$. ($\mu_r = 0$, $\mu_s = 0.275$)

Based on the mean particle velocity $\langle v \rangle$ in Fig. 7, the particle Stokes number in riser flows St = $\rho_p d_p (U - \langle v \rangle)/\mu_g$ [85] is evaluated to be ~ 3,000, indicating the dominance of particle inertia over fluid viscous force and the importance of interparticle collisions in affecting the flow behavior. Therefore, by conducting an analysis on the particle collisions statistics, we found the decreasing $\langle N_{agg} \rangle$ and $\langle n_{agg} \rangle$ with increasing e observed in Fig. 7 can be attributed to the reduced probability of agglomerating collisions. More specifically, Fig. 8 summarizes the statistical distributions collected as two particles collides in riser flows. The inset of Fig. 8a is a schematic of a binary collision, which illustrates the normal impact velocity for approaching collisions $v_{im,n}$ and impact angle θ for a collision. Fig. 8a shows the distribution of the number of particles involved in collisions n_{coll}. Due to the small solid concentration $\varepsilon_s = 0.01$ in riser flows, the mean free path of particles is much larger than particles in defluidization. Thus, the frequency for multiple-particle collisions drops quickly with increasing n_{coll} and binary collisions (n_{coll} = 2) dominate the particle collisions in riser flows. For a binary collision, it is known that when $v_{im,n} \le v_{crit}$, where v_{crit} is the critical agglomeration velocity, the collision will result in agglomeration and a doublet will form [86-89]. As a result of reduced collisional dissipation, Fig. 8b indicates that increasing e causes a decrease in v_{crit} at typical impact angles θ. The distributions of θ show peaks at 45° but have little independence on varying e (inset of Fig. 8b), suggesting level of energy dissipation does not alter the geometric configurations of particle collisions in riser flows. With v_{crit} known, the probability of agglomerating binary collisions P_{agg} can be evaluated by $P_{agg} = \int_0^{v_{crit}} f(v_{im,n}) dv_{im,n}$, where $f(v_{im,n})$ is the distribution of normal impact velocity. The distributions $f(v_{im,n})$ collected in simulations are summarized in Fig. 8c, where changing e is seen to have relatively small impact on $f(v_{im,n})$. Therefore, with a decreasing v_{crit}, P_{agg} drops from 25% to 0.3% (evaluated using v_{crit} values at $\theta = 45°$, red curve in Fig. 8b) as e increases from 0.4 to 0.99 (inset of Fig. 8c). An example of P_{agg} at $e = 0.4$ is illustrated by the shaded area in Fig. 8c. Since a smaller P_{agg} indicates a reduced fraction of binary collisions that end up in doublets, $\langle N_{agg} \rangle$ decreases with increasing e. Similarly, the mean critical agglomeration velocities for collisions with $n_{coll} \geq 3$ is likely to be decreased with increasing e (though such critical velocities also depend on the geometric configuration of collisions and are non-unique for each specified e [90]), resulting a decrease in $\langle n_{agg} \rangle$ at higher e. Given the correlation between v_{crit} and $\langle n_{agg} \rangle$ discussed above, it is reasonable that changing material stiffness or Tabor parameter of particles, which alters v_{crit} [15,91], affects particle agglomeration in riser flows as well [16]. It is worth mentioning that assuming the fluctuating velocities ($\mathbf{v}' = \mathbf{v} - \langle \mathbf{v} \rangle$) of all particles in risers follow Gaussian distribution with identical "granular temperature $T = 1/3\langle |\mathbf{v} - \langle \mathbf{v} \rangle|^2 \rangle$", the normal impact velocity $v_{im,n}$ follows Rayleigh distribution $f_M(v_{im,n}) = v_{im,n} / (2T) \exp[-v_{im,n}^2 / (4T)]$. However, as shown in Fig. 8c, $f(v_{im,n})$ has higher tails than the best fit using $f_M(v_{im,n})$ (red dashed line in Fig. 8c) at $e = 0.6$ (higher tails also seen for other values of e). This deviation of $f(v_{im,n})$ from $f_M(v_{im,n})$ is reminiscent of granular gases, in which higher tails of velocity distributions than Gaussian are observed and proven to be a consequence of particle clustering due to inelastic collisions [92-94]. Since cohesion enhances particle clustering by forming agglomerates, deviation of $f(v_{im,n})$ from $f_M(v_{im,n})$ in the current system is expected. Recently, Murphy and Subramaniam [95] conducted DEM simulations for a granular gas of cohesive particles. A wider normal relative velocity distribution than Gaussian is also observed.

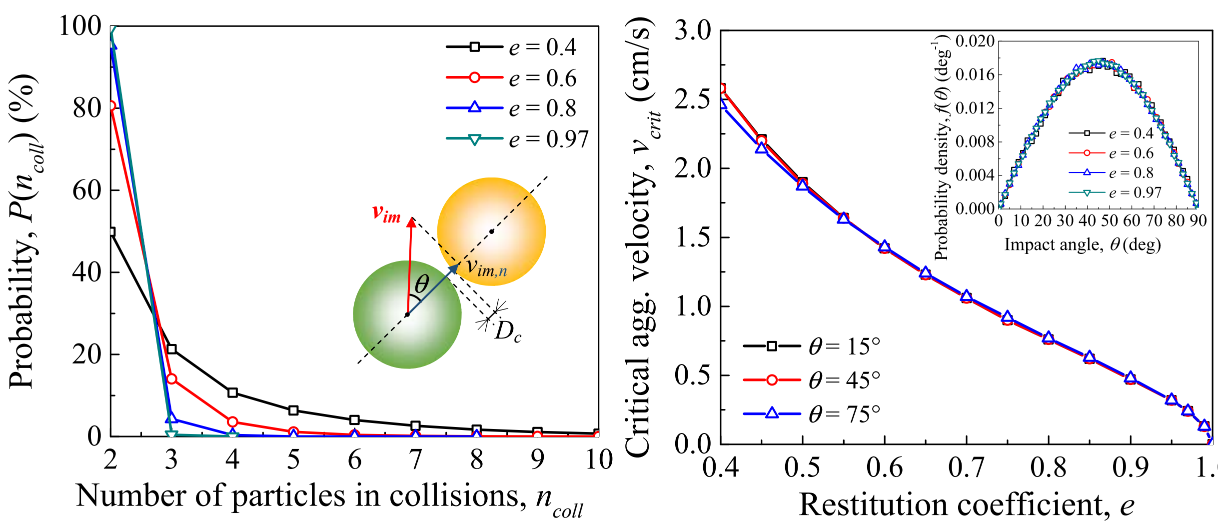

(a) (b)

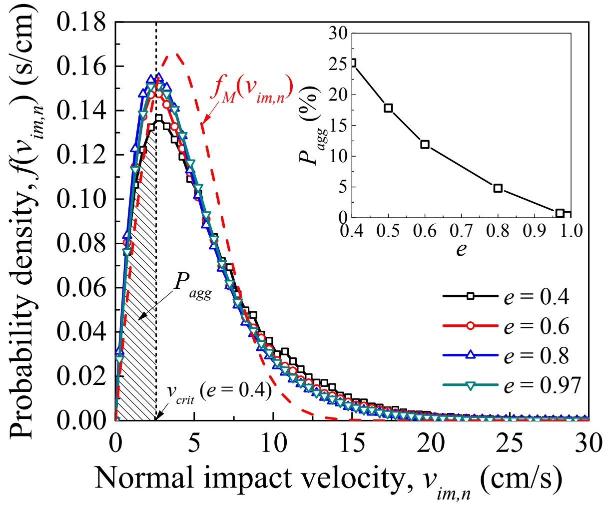

(c)

Fig. 8. (a) Probability mass function of the number of particles involved in collisions in riser flows with n_{coll} = 2 standing for the binary collision (inset: an oblique binary collision with normal impact velocity $v_{im,n}$ and impact angle θ collected right before they enter the cohesive well D_c.) (Refer to Section 2.2 for the definition of D_c); (b) critical agglomeration velocity in binary collisions as a function of e (inset: distributions of impact angle at different e); (c) distributions of normal impact velocity at different e (μ_s = 0.275, μ_r = 0) (red dashed line: prediction of velocity distribution at e = 0.6, inset: probability of agglomerating binary collisions with increasing e).

3.2.2 Effect of friction

Simulations were also conducted by changing μ_s or μ_r at e = 0.97. In contrast to the defluidization discussed in section 3.1.1, neither μ_s nor μ_r affects the average particle speed and agglomerate properties in riser flows (results not shown for brevity). Similar to the discussion in Section 3.2.1, the insensitivity of agglomerates to varying particle friction can be attributed to the fact that v_{crit} is unaffected by either μ_s or μ_r, as shown in Fig. 9. With a constant v_{crit}, the probability of agglomerating collisions remains unchanged as well as the agglomerate properties.

A physical understanding of Fig. 9 is as follows: since agglomeration is determined by cohesion that acts only in the normal direction of interacting particles, the role of the dynamics associated with tangential motions controlled by μ_s and μ_r is minimized. A similar explanation applies to the insensitivity of v_{crit} to varying impact angle in Fig. 8b. Fig. 9 also confirmed previous findings that for binary collisions, the relative motion of particles in the tangential direction has little impact on that in the normal direction, which was seen for non-cohesive particles in ambient conditions [66] or submerged in liquids [96] as well as wetted particles [97]. Therefore, smoothing particles to decrease friction may not help avoid agglomeration in risers if the particle restitution coefficient remains the same. Conversely, since cohesion usually increases with decreasing surface roughness, agglomeration can be enhanced with smoothed particles.

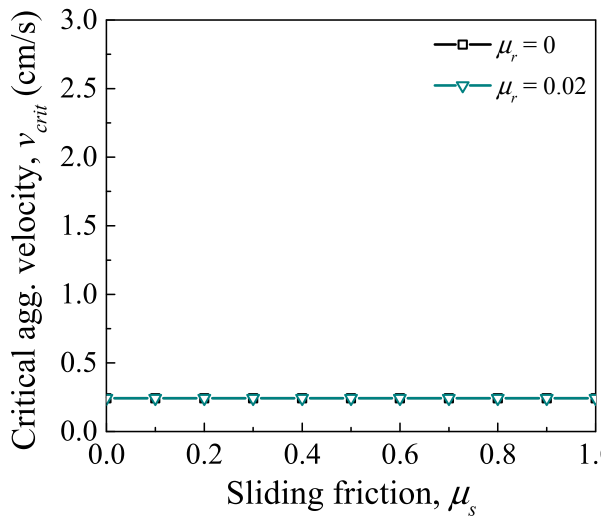

Fig. 9. Critical agglomeration velocity in binary collisions as a function of μ_s with varying μ_r. ($e = 0.97$)

4 Conclusions

From DEM-CFD simulations, a reverse sensitivity to friction and restitution coefficient in gas-solid flows of cohesive particles was observed between dense and dilute flows. Namely, particle defluidization is more influenced by friction since the flow is dense with lasting particle contacts. Conversely, particle velocity and agglomerates in dilute riser flow are dictated by the restitution coefficient due to the influence of inelastic dissipation on the critical agglomeration velocity of binary collisions. At lower rolling friction, an increase in sliding friction shows a non-monotonic effect on particle defluidization, which can be attributed to shift of the principal role of sliding friction from enhanced sliding dissipation to increased driving for particle spin. The different sensitivities suggest the complexity of the continuum modeling for gas-solid flows can be reduced provided the leading factor in the system of interest is properly considered. The results of this work may also serve as validation data for predictions from continuum models incorporating particle cohesion and friction.

Acknowledgements

The authors are grateful for the financial support provided by the Dow Corning Corporation. This work utilized the Janus supercomputer, which is supported by the National Science Foundation (award number CNS-0821794) and the University of Colorado Boulder. The Janus supercomputer is a joint effort of the University of Colorado Boulder, the University of Colorado Denver and the National Center for Atmospheric Research. Janus is operated by the University of Colorado Boulder.

Appendix: Theoretical analysis on the competing effects of sliding friction

To establish an analytical understanding of the competing effects associated with changes in sliding friction (μ_s), we simplify the behavior of a single particle p during defluidization into two processes (Fig. 10): (i) acceleration of the particle after a binary collision characteristic of the bubbling regimes with relatively low solid concentration and (ii) deceleration and eventual stoppage as the particle slides or rolls on a solid wall, mimicking the condition of enduring contacts as $U \rightarrow U_{cf}$. Based on the post-collisional velocities (translational and angular) of the particle obtained from Process I, the non-monotonic effect of μ_s will be demonstrated by variation of the particle stop distances (the distance travelled by the particle before it stops on the rough wall with the same μ_s and μ_r as the particle) in Process II with increasing μ_s. Two stop distances will be computed, based on assumptions of pure sliding (D_s) and pure rolling (D_r) respectively, as shown in Fig. 10b.

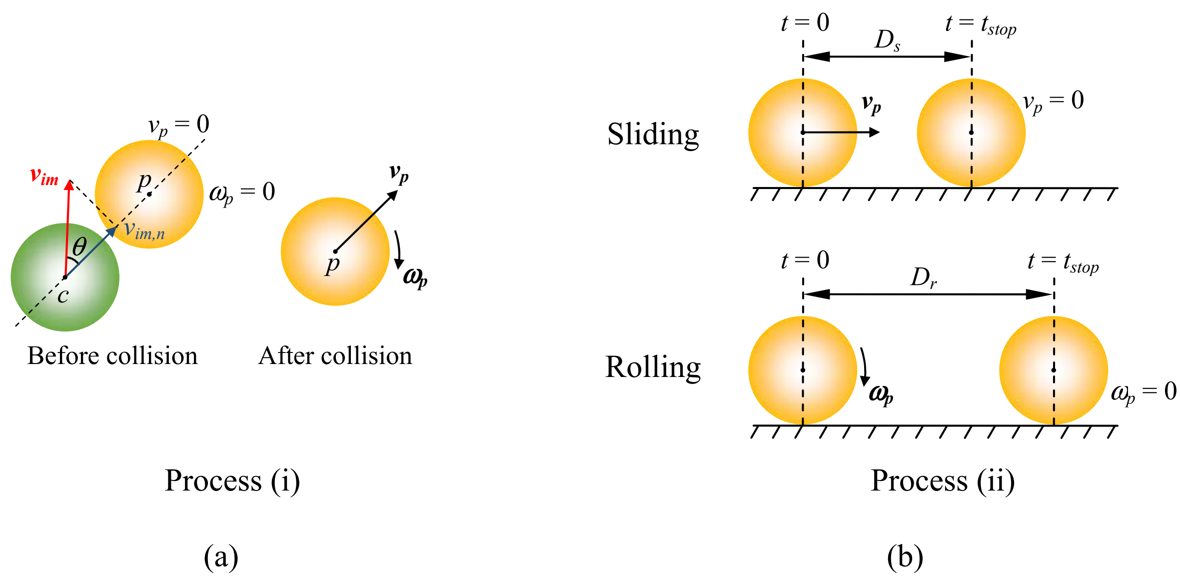

Fig. 10. Illustration of the two processes of a single particle p considered in theoretical analysis: (i) binary collision during which the initially static particle p (yellow) gains translational velocity v_p and angular velocity ω_p after collision, and (ii) particle either sliding or rolling on a rough solid wall with the initial velocities as the translational velocity and rotational velocity after Process I, respectively.

To calculate the post-collisional velocities of the initially static particle p with particle c possessing impact velocity v_{im} and impact angle θ (Fig. 10a), we extend the theory by Foerster et al [66] to cohesive particles with rolling friction. During the collision, the linear and angular momentum balances are given by

$$
\begin{aligned}
m\mathbf{v}_p &= \mathbf{J}_c \\
I\boldsymbol{\omega}_p &= \frac{d_p[\hat{\mathbf{n}} \times \mathbf{J}_c + \mathbf{J}_r)]}{2}
\end{aligned}
\tag{A1}
$$

where $\mathbf{v}_p$, $\boldsymbol{\omega}_p$ are respectively, the translational and angular velocities after the collision, $\hat{\mathbf{n}}$ is unit normal vector pointing from the center of particle c to particle p. $\mathbf{J}_c$ and $\mathbf{J}_r$ are the momentum transfer from contact forces and rolling friction during the collision, respectively given by

$$\mathbf{J}_c = \begin{cases} \dfrac{m(1+e)}{2} v_{im} \cos\theta \hat{\mathbf{n}} + \dfrac{\mu_s m(1+e)}{2} v_{im} \cos\theta \hat{\mathbf{t}} + \mu_s \,\mathrm{Bo}\, mgt_{cb} \hat{\mathbf{t}} & \mu_s \le \mu_{s,crit} \\ \dfrac{m(1+e)}{2} v_{im} \cos\theta \hat{\mathbf{n}} + \dfrac{m}{7}(1+\beta) v_{im} \sin\theta \hat{\mathbf{t}} & \mu_s > \mu_{s,crit} \end{cases} \quad \text{(A2)}$$

$$\mathbf{J}_r = -\frac{\mu_r m(1+e)}{2} v_{im} \cos\theta \hat{\mathbf{t}} - \mu_r \,\mathrm{Bo}\, mgt_{cb} \hat{\mathbf{t}}$$

where $\hat{\mathbf{t}} = (\mathbf{v}_{im} - v_{im}\cos\theta\hat{\mathbf{n}})/(v_{im}\sin\theta)$ is tangential unit vector and Bo = $F_{vdW}(D_c)/mg$ is the granular Bond number of cohesion. $\mu_{s,crit} = 2(1+\beta)v_{im}\sin\theta / \{7[(1+e)v_{im}\cos\theta + 2\,\mathrm{Bo}\, gt_{cb}]\}$ is the critical μ_s governs the onset of "non-sliding" [66] with β being the tangential restitution coefficient. t_{cb} is the binary collision duration obtained by Timoshenko [98]

$$t_{cb} = \frac{2.214 d_p}{(v_{im}\cos\theta)^{1/5}} \left(\frac{\rho_p}{E}\right)^{2/5} \quad \text{(A3)}$$

Combining the Eq. (A1) and (A2), the magnitudes of the translational velocity v_p and angular velocity ω_p of particle p after the oblique collision are respectively given by

$$v_p = \begin{cases} \sqrt{\left[\dfrac{1}{2}\mu_s(1+e)v_{im}\cos\theta + \mu_s \,\mathrm{Bo}\, gt_{cb}\right]^2 + \left[\dfrac{1}{2}(1+e)v_{im}\cos\theta\right]^2} & \mu_s \le \mu_{s,crit} \\ \sqrt{\left(\dfrac{1}{7}(1+\beta)v_{im}\sin\theta\right)^2 + \left[\dfrac{1}{2}(1+e)v_{im}\cos\theta\right]^2} & \mu_s > \mu_{s,crit} \end{cases} \quad \text{(A4)}$$

$$\omega_p = \begin{cases} \dfrac{5(\mu_s - \mu_r)\left[(1+e)v_{im}\cos\theta + 2\,\mathrm{Bo}\, gt_{cb}\right]}{2d_p} & \mu_s \le \mu_{s,crit} \\ \dfrac{5(1+\beta)v_{im}\sin\theta}{7d_p} - \dfrac{5\mu_r(1+e)v_{im}\cos\theta}{2d_p} - \dfrac{5\mu_r \,\mathrm{Bo}\, gt_{cb}}{d_p} & \mu_s > \mu_{s,crit} \end{cases} \quad \text{(A5)}$$

Using the velocities calculated by Eq. (A4) and Eq. (A5) as initial conditions, the stop distances for the particle under the assumptions of pure sliding D_s and pure rolling D_r are respectively computed as

$$D_s = \frac{v_p^2}{2\mu_s g(1+Bo)} \quad \text{(A6)}$$

$$D_r = \frac{\mu_s d_p^2 \omega_p^2}{10\mu_r g(7\mu_s + 5\mu_r)(1+Bo)} \quad \text{(A7)}$$

where $dD_s/d\mu_s < 0$ while $dD_r/d\mu_s > 0$ for $\mu_s > \mu_{s,crit}$. Therefore, when μ_s is small ($\mu_s < \mu_{s,crit}$), increasing μ_s has the opposite effect on D_s and D_r, i.e. D_s decreases and D_r increases. For the case of defluidization, as U reduces towards U_{cf}, the complex many-body interactions likely results in lasting contacts that are neither pure sliding nor pure rolling but a mixture of the two, and thus the combined stop distance $D_s + D_r$ is a reasonable quantity to measure the overall effect of μ_s. Based on the material properties in this work with v_{im} = 5 cm/s and θ = 75° (typical values in fluidized beds), $D_s + D_r$ is plotted against μ_s in Fig. 11. At $\mu_r = 0.002$, for smaller μ_s (< 0.1), the decreasing D_s due to increased μ_s causes a quick decay of $D_s + D_r$, while increased D_r with larger ω_p (see Eq. (A5)) leads to a growth of $D_s + D_r$ as μ_s is further increased (> 0.1), until $\mu_s > \mu_{s,crit}$ (≈ 0.5), when $D_s + D_r$ levels off upon the translation to "non-sliding". With increased $\mu_r = 0.02$, particle angular velocity ω_p is significantly limited (see Eq. (A5)), so that $D_s + D_r$ is behaving closer to a monotonic decreasing (i.e., D_s is the dominant term). Since a larger $D_s + D_r$ suggests a higher mobility for particles to rearrange into a denser packing and result in a smaller U_{cf}, the variation of $D_s + D_r$ with μ_s is consistent with the behavior of U_{cf} with μ_s in Fig. 3, where a non-monotonic trend is observed at smaller μ_r and U_{cf} generally levels off when $\mu_s > 0.5$. In sum, by analyzing the dynamics of an individual particle in representative processes, the competing effects of sliding friction found in the many-particle defluidization are recovered.

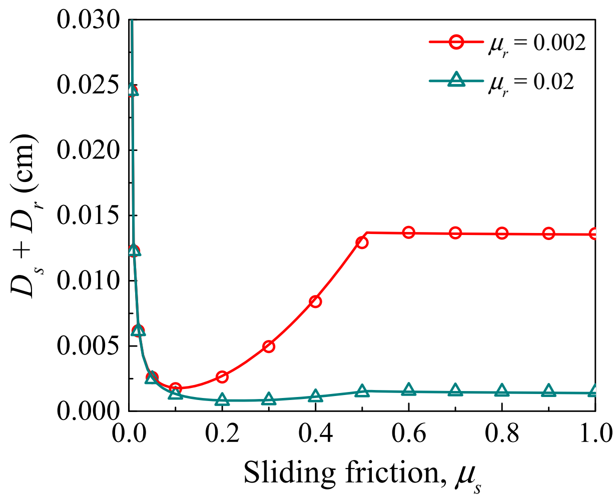

Fig. 11. Combined stop distance in Process (ii) for particle p moving on a wall with the same μ_s and μ_r as the particle. The material properties used in calculations are listed in Table 1 with v_{im} = 5 cm/s, θ = 75°, β is assumed to be 0 for $\mu_s > \mu_{s,crit}$ [99] and Bo = 5.43. Note e = 0.96, which is the effective e for cohesive binary collisions with input e = 0.97 in the simulations [34]. (Solid lines: sum of Eq. (A6) and Eq. (A7), symbols: DEM simulations)

References

[1] D. Kunii and O. Levenspiel, *Fluidization engineering* (Butterworth-Heinemann, Boston, 1991).

[2] L.-S. Fan and C. Zhu, *Principles of gas-solid flows* (Cambridge University Press, Cambridge ; New York, 1998).

[3] S. Tenneti and S. Subramaniam, Particle-Resolved Direct Numerical Simulation for Gas-Solid Flow Model Development, Annu. Rev. Fluid Mech. **46**, 199 (2014).

[4] M. A. van der Hoef, M. V. Annaland, N. G. Deen, and J. A. M. Kuipers, Numerical simulation of dense gas-solid fluidized beds: A multiscale modeling strategy, Annu. Rev. Fluid Mech. **40**, 47 (2008).

[5] T. W. Li, J. F. Dietiker, and L. Shadle, Comparison of full-loop and riser-only simulations for a pilot-scale circulating fluidized bed riser, Chem. Eng. Sci. **120**, 10 (2014).

[6] H. T. Bi, N. Ellis, I. A. Abba, and J. R. Grace, A state-of-the-art review of gas-solid turbulent fluidization, Chem. Eng. Sci. **55**, 4789 (2000).

[7] J. W. Chew, D. M. Parker, and C. M. Hrenya, Elutriation and Species Segregation Characteristics of Polydisperse Mixtures of Group B Particles in a dilute CFB Riser, AIChE J. **59**, 84 (2013).

[8] S. C. Tsinontides and R. Jackson, The mechanics of gas fluidized beds with an interval of stable fluidization, J. Fluid Mech. **255**, 237 (1993).

[9] M. J. Rhodes, X. S. Wang, M. Nguyen, P. Stewart, and K. Liffman, Use of discrete element method simulation in studying fluidization characteristics: influence of interparticle force, Chem. Eng. Sci. **56**, 69 (2001).

[10] F. Yang, C. Thornton, and J. Seville, Effect of surface energy on the transition from fixed to bubbling gas-fluidised beds, Chem. Eng. Sci. **90**, 119 (2013).

[11] O. Oke, P. Lettieri, and L. Mazzei, An investigation on the mechanics of homogeneous expansion in gas-fluidized beds, Chem. Eng. Sci. **127**, 95 (2015).

[12] M. Ye, M. A. van der Hoef, and J. A. M. Kuipers, The effects of particle and gas properties on the fluidization of Geldart A particles, Chem. Eng. Sci. **60**, 4567 (2005).

[13] M. W. Weber and C. M. Hrenya, Computational study of pressure-drop hysteresis in fluidized beds, Powder Technol. **177**, 170 (2007).

[14] T. Mikami, H. Kamiya, and M. Horio, Numerical simulation of cohesive powder behavior in a fluidized bed, Chem. Eng. Sci. **53**, 1927 (1998).

[15] T. Kobayashi, T. Tanaka, N. Shimada, and T. Kawaguchi, DEM-CFD analysis of fluidization behavior of Geldart Group A particles using a dynamic adhesion force model, Powder Technol. **248**, 143 (2013).

[16] M. H. Zhang, K. W. Chu, F. Wei, and A. B. Yu, A CFD-DEM study of the cluster behavior in riser and downer reactors, Powder Technol **184**, 151 (2008).

[17] M. Wang, W. B. Zhu, Q. Q. Sun, and X. B. Zhang, A DEM simulation of dry and wet particle flow behaviors in riser, Powder Technol. **267**, 221 (2014).

[18] M. Girardi, S. Radl, and S. Sundaresan, Simulating wet gas–solid fluidized beds using coarse-grid CFD-DEM, Chem. Eng. Sci. **144**, 224 (2016).

[19] C. Mangwandi, Y. S. Cheong, M. J. Adams, M. J. Hounslow, and A. D. Salman, The coefficient of restitution of different representative types of granules, Chem. Eng. Sci. **62**, 437 (2007).

[20] M. J. V. Goldschmidt, J. A. M. Kuipers, and W. P. M. van Swaaij, Hydrodynamic modelling of dense gas-fluidised beds using the kinetic theory of granular flow: effect of coefficient of restitution on bed dynamics, Chem. Eng. Sci. **56**, 571 (2001).

[21] N. Reuge, L. Cadoret, C. Coufort-Saudejaud, S. Pannala, M. Syamlal, and B. Caussat, Multifluid Eulerian modeling of dense gas-solids fluidized bed hydrodynamics: Influence of the dissipation parameters, Chem. Eng. Sci. **63**, 5540 (2008).

[22] M. S. van Buijtenen, N. G. Deen, S. Heinrich, S. Antonyuk, and J. A. M. Kuipers, Discrete Particle Simulation Study on the Influence of the Restitution Coefficient on Spout Fluidized-Bed Dynamics, Chem. Eng. Technol. **32**, 454 (2009).

[23] B. P. B. Hoomans, J. A. M. Kuipers, W. J. Briels, and W. P. M. vanSwaaij, Discrete particle simulation of bubble and slug formation in a two-dimensional gas-fluidised bed: A hard-sphere approach, Chem. Eng. Sci. **51**, 99 (1996).

[24] J. Li and J. A. M. Kuipers, Effect of competition between particle-particle and gas-particle interactions on flow patterns in dense gas-fluidized beds, Chem. Eng. Sci. **62**, 3429 (2007).

[25] I. Goldhirsch and G. Zanetti, Clustering instability in dissipative gases, Phys. Rev. Lett. **70**, 1619 (1993).

[26] Y. F. Wang, Z. X. Chao, and H. A. Jakobsen, A Sensitivity Study of the Two-Fluid Model Closure Parameters (β, e) Determining the Main Gas-Solid Flow Pattern Characteristics, Ind. Eng. Chem. Res. **49**, 3433 (2010).

[27] F. Gollwitzer, I. Rehberg, C. A. Kruelle, and K. Huang, Coefficient of restitution for wet particles, Phys. Rev. E **86**, 011303 (2012).

[28] Q. F. Hou, Z. Y. Zhou, and A. B. Yu, Micromechanical modeling and analysis of different flow regimes in gas fluidization, Chem. Eng. Sci. **84**, 449 (2012).

[29] J. E. Galvin and S. Benyahia, The Effect of Cohesive Forces on the Fluidization of Aeratable Powders, AIChE J. **60**, 473 (2014).

[30] R. Wilson, D. Dini, and B. van Wachem, A numerical study exploring the effect of particle properties on the fluidization of adhesive particles, AIChE J. **62**, 1467 (2016).

[31] M. Ye, M. A. van der Hoef, and J. A. M. Kuipers, A numerical study of fluidization behavior of Geldart A particles using a discrete particle model, Powder Technol. **139**, 129 (2004).

[32] J. K. Pandit, X. S. Wang, and M. J. Rhodes, On Geldart Group A behaviour in fluidized beds with and without cohesive interparticle forces: A DEM study, Powder Technol. **164**, 130 (2006).

[33] J. R. Royer, D. J. Evans, L. Oyarte, Q. Guo, E. Kapit, M. E. Mobius, S. R. Waitukaitis, and H. M. Jaeger, High-speed tracking of rupture and clustering in freely falling granular streams, Nature **459**, 1110 (2009).

[34] P. Liu, C. Q. LaMarche, K. M. Kellogg, and C. M. Hrenya, Fine-particle defluidization: Interaction between cohesion, Young's modulus and static bed height, Chem. Eng. Sci. **145**, 266 (2016).

[35] J. T. Jenkins and M. W. Richman, Kinetic theory for plane flows of a dense gas of identical, rough, inelastic, circular disks, Phys. Fluids **28**, 3485 (1985).

[36] H. Kim and H. Arastoopour, Extension of kinetic theory to cohesive particle flow, Powder Technol. **122**, 83 (2002).

[37] R. Fan, D. L. Marchisio, and R. O. Fox, Application of the direct quadrature method of moments to polydisperse gas-solid fluidized beds, Powder Technol. **139**, 7 (2004).

[38] P. Jop, Y. Forterre, and O. Pouliquen, A constitutive law for dense granular flows, Nature **441**, 727 (2006).

[39] B. van Wachem and S. Sasic, Derivation, simulation and validation of a cohesive particle flow CFD model, AIChE J. **54**, 9 (2008).

[40] S. Chialvo and S. Sundaresan, A modified kinetic theory for frictional granular flows in dense and dilute regimes, Phys. Fluids **25**, 070603 (2013).

[41] A. H. A. Motlagh, J. R. Grace, M. Salcudean, and C. M. Hrenya, New structure-based model for Eulerian simulation of hydrodynamics in gas-solid fluidized beds of Geldart group "A" particles, Chem. Eng. Sci. **120**, 22 (2014).

[42] F. P. Beer and E. R. Johnston, *Mechanics for engineers: statics and dynamics* (McGraw-Hill, New York, 1976).

[43] Y. C. Zhou, B. D. Wright, R. Y. Yang, B. H. Xu, and A. B. Yu, Rolling friction in the dynamic simulation of sandpile formation, Physica A **269**, 536 (1999).

[44] Y. Tsuji, T. Tanaka, and T. Ishida, Lagrangian numerical simulation of plug flow of cohesionless particles in a horizontal pipe, Powder Technol. **71**, 239 (1992).

[45] D. Antypov and J. A. Elliott, On an analytical solution for the damped Hertzian spring, Europhys. Lett. **94**, 50004 (2011).

[46] C. Q. LaMarche, S. Leadley, P. Liu, K. M. Kellogg, and C. M. Hrenya, Method of quantifying surface roughness for accurate adhesive force predictions, Chem. Eng. Sci. **158**, 140 (2017).

[47] J. N. Israelachvili, *Intermolecular and surface forces* (Academic Press, Burlington, MA, 2011).

[48] Y. Guo and J. S. Curtis, Discrete Element Method Simulations for Complex Granular Flows, Annu. Rev. Fluid Mech. **47**, 21 (2015).

[49] R. J. Hill, D. L. Koch, and A. J. C. Ladd, The first effects of fluid inertia on flows in ordered and random arrays of spheres, J. Fluid Mech. **448**, 213 (2001).

[50] R. J. Hill, D. L. Koch, and A. J. C. Ladd, Moderate-Reynolds-number flows in ordered and random arrays of spheres, J. Fluid Mech. **448**, 243 (2001).

[51] S. Benyahia, M. Syamlal, and T. J. O'Brien, Extension of Hill-Koch-Ladd drag correlation over all ranges of Reynolds number and solids volume fraction, Powder Technol. **162**, 166 (2006).

[52] S. V. Patankar, *Numerical heat transfer and fluid flow* (Hemisphere Pub. Corp. McGraw-Hill, Washington, New York, 1980).

[53] C. Q. LaMarche, P. Liu, K. M. Kellogg, A. W. Weimer, and C. M. Hrenya, A system-size independent validation of CFD-DEM for noncohesive particles, AIChE J. **61**, 4051 (2015).

[54] Y. Z. Zhao, Y. Cheng, C. N. Wu, Y. L. Ding, and Y. Jin, Eulerian-Lagrangian simulation of distinct clustering phenomena and RTDs in riser and downer, Particuology **8**, 44 (2010).

[55] N. Taberlet, P. Richard, and E. J. Hinch, S shape of a granular pile in a rotating drum, Phys. Rev. E **73**, 050301 (2006).

[56] P. Philippe and M. Badiane, Localized fluidization in a granular medium, Phys. Rev. E **87**, 042206 (2013).

[57] B. Herb, S. Dou, K. Tuzla, and J. C. Chen, Solid mass fluxes in circulating fluidized beds, Powder Technol. **70**, 197 (1992).

[58] S. Benyahia, H. Arastoopour, T. M. Knowlton, and H. Massah, Simulation of particles and gas flow behavior in the riser section of a circulating fluidized bed using the kinetic theory approach for the particulate phase, Powder Technol. **112**, 24 (2000).

[59] J. McMillan, F. Shaffer, B. Gopalan, J. W. Chew, C. Hrenya, R. Hays, S. B. R. Karri, and R. Cocco, Particle cluster dynamics during fluidization, Chem. Eng. Sci. **100**, 39 (2013).

[60] A. Castellanos, The relationship between attractive interparticle forces and bulk behaviour in dry and uncharged fine powders, Adv. Phys. **54**, 263 (2005).

[61] J. Capecelatro, O. Desjardins, and R. O. Fox, On fluid-particle dynamics in fully developed cluster-induced turbulence, J. Fluid Mech. **780**, 578 (2015).

[62] P. J. Blau, *Friction science and technology from concepts to applications* (CRC Press, Boca Raton, FL, 2009).

[63] W. R. Ketterhagen, R. Bharadwaj, and B. C. Hancock, The coefficient of rolling resistance (CoRR) of some pharmaceutical tablets, Int. J. Pharm. **392**, 107 (2010).

[64] ASTM, Standard Test Method for Measuring Rolling Friction Characteristics of a Spherical Shape on a Flat Horizontal Plane, G194-08, American Society for Testing and Materials, West Conshohocken, PA (2013).

[65] G. Kuwabara and K. Kono, Restitution coefficient in a collision between two spheres, Jpn. J. Appl. Phys. Part 1 - Regul. Pap. Short Notes Rev. Pap. **26**, 1230 (1987).

[66] S. F. Foerster, M. Y. Louge, A. H. Chang, and K. Allia, Measurements of the collision properties of small spheres, Phys. Fluids **6**, 1108 (1994).

[67] M. Syamlal, W. Rogers, and T. J. O'Brien, MFIX Documentation Theory Guide, (1993).

[68] C. Q. LaMarche, A. W. Miller, P. Liu, and C. M. Hrenya, Linking micro-scale predictions of capillary forces to macro-scale fluidization experiments in humid environments, AIChE J. **62**, 3585 (2016).

[69] H. A. Makse, D. L. Johnson, and L. M. Schwartz, Packing of compressible granular materials, Phys. Rev. Lett. **84**, 4160 (2000).

[70] R. Y. Yang, R. P. Zou, and A. B. Yu, Effect of material properties on the packing of fine particles, J. Appl. Phys. **94**, 3025 (2003).

[71] G. R. Farrell, K. M. Martini, and N. Menon, Loose packings of frictional spheres, Soft Matter **6**, 2925 (2010).

[72] R. Moreno-Atanasio, B. H. Xu, and M. Ghadiri, Computer simulation of the effect of contact stiffness and adhesion on the fluidization behaviour of powders, Chem. Eng. Sci. **62**, 184 (2007).

[73] M. J. V. Goldschmidt, R. Beetstra, and J. A. M. Kuipers, Hydrodynamic modelling of dense gas-fluidised beds: comparison and validation of 3D discrete particle and continuum models, Powder Technol. **142**, 23 (2004).

[74] Y. H. Zhao, B. Lu, and Y. J. Zhong, Influence of collisional parameters for rough particles on simulation of a gas-fluidized bed using a two-fluid model, Int. J. Multiph. Flow **71**, 1 (2015).

[75] I. Goldhirsch, Rapid granular flows, Annu. Rev. Fluid Mech. **35**, 267 (2003).

[76] W. D. Fullmer and C. M. Hrenya, The Clustering Instability in Rapid Granular and Gas-Solid Flows, Annu. Rev. Fluid Mech. **49** (2017).

[77] K. M. Kellogg, P. Liu, C. Q. LaMarche, and C. M. Hrenya, Continuum Theory for Rapid, Cohesive-Particle Flows: Balance Equations and DEM-based Closure of Cohesion-specific Quantities (submitted), J. Fluid Mech.

[78] M. A. Van der Hoef, R. Beetstra, and J. A. M. Kuipers, Lattice-Boltzmann simulations of low-Reynolds-number flow past mono- and bidisperse arrays of spheres: results for the permeability and drag force, J. Fluid Mech. **528**, 233 (2005).

[79] K. Agrawal, P. N. Loezos, M. Syamlal, and S. Sundaresan, The role of meso-scale structures in rapid gas-solid flows, J. Fluid Mech. **445**, 151 (2001).

[80] F. Shaffer, B. Gopalan, R. W. Breault, R. Cocco, S. B. R. Karri, R. Hays, and T. Knowlton, High speed imaging of particle flow fields in CFB risers, Powder Technol. **242**, 86 (2013).

[81] M. Mehrabadi, E. Murphy, and S. Subramaniam, Development of a gas-solid drag law for clustered particles using particle-resolved direct numerical simulation, Chem. Eng. Sci. **152**, 199 (2016).

[82] M. T. Shah, R. P. Utikar, M. O. Tade, G. M. Evans, and V. K. Pareek, Effect of a cluster on gas-solid drag from lattice Boltzmann simulations, Chem. Eng. Sci. **102**, 365 (2013).

[83] G. F. Zhou, Q. G. Xiong, L. M. Wang, X. W. Wang, X. X. Ren, and W. Ge, Structure-dependent drag in gas-solid flows studied with direct numerical simulation, Chem. Eng. Sci. **116**, 9 (2014).

[84] T. Li, L. Wang, W. Rogers, G. Zhou, and W. Ge, An approach for drag correction based on the local heterogeneity for gas–solid flows, **63**, 1203 (2017).

[85] J. W. Chew, R. Hays, J. G. Findlay, T. M. Knowlton, S. B. R. Karri, R. A. Cocco, and C. M. Hrenya, Reverse core-annular flow of Geldart Group B particles in risers, Powder Technol. **221**, 1 (2012).

[86] P. Gondret, M. Lance, and L. Petit, Bouncing motion of spherical particles in fluids, Phys. Fluids **14**, 643 (2002).

[87] M. W. Weber, D. K. Hoffman, and C. M. Hrenya, Discrete-particle simulations of cohesive granular flow using a square-well potential, Granul. Matter **6**, 239 (2004).

[88] A. A. Kantak, C. M. Hrenya, and R. H. Davis, Initial rates of aggregation for dilute, granular flows of wet particles, Phys. Fluids **21**, 023301 (2009).

[89] C. M. Donahue, C. M. Hrenya, and R. H. Davis, Stokes's Cradle: Newton's Cradle with Liquid Coating, Phys. Rev. Lett. **105**, 034501 (2010).

[90] P. Liu, K. M. Kellogg, C. Q. LaMarche, and C. M. Hrenya, Dynamics of singlet-doublet collisions of cohesive particles (submitted), Chem. Eng. J.

[91] E. Murphy and S. Subramaniam, Binary collision outcomes for inelastic soft-sphere models with cohesion, Powder Technol. **305**, 462 (2017).

[92] A. Puglisi, V. Loreto, U. M. B. Marconi, A. Petri, and A. Vulpiani, Clustering and non-Gaussian behavior in granular matter, Phys. Rev. Lett. **81**, 3848 (1998).

[93] W. Losert, D. G. W. Cooper, J. Delour, A. Kudrolli, and J. P. Gollub, Velocity statistics in excited granular media, Chaos **9**, 682 (1999).

[94] J. S. van Zon and F. C. MacKintosh, Velocity distributions in dissipative granular gases, Phys. Rev. Lett. **93** (2004).

[95] E. Murphy and S. Subramaniam, Freely cooling granular gases with short-ranged attractive potentials, Phys. Fluids **27**, 043301 (2015).

[96] F. L. Yang and M. L. Hunt, Dynamics of particle-particle collisions in a viscous liquid, Phys. Fluids **18**, 121506 (2006).

[97] C. M. Donahue, R. H. Davis, A. A. Kantak, and C. M. Hrenya, Mechanisms for agglomeration and deagglomeration following oblique collisions of wet particles, Phys. Rev. E **86**, 021303 (2012).

[98] S. Timoshenko, *Theory of elasticity* (McGraw-Hill, New York, 1934).

[99] T. Schwager, V. Becker, and T. Poschel, Coefficient of tangential restitution for viscoelastic spheres, Eur. Phys. J. E **27**, 107 (2008).